Monthly Notices
of the
ROYAL ASTRONOMICAL SOCIETY

MNRAS **482,** 2838–2851 (2019)
Advance Access publication 2018 October 23

doi:10.1093/mnras/sty2858

Intracluster light: a luminous tracer for dark matter in clusters of galaxies

Mireia Montes [1,2]★ and Ignacio Trujillo[3,4]

[1]*School of Physics, University of New South Wales, Sydney, NSW 2052, Australia*
[2]*Department of Astronomy, Yale University, New Haven, CT 06511, USA*
[3]*Instituto de Astrofísica de Canarias, c/ Vía Láctea s/n, E-38205 La Laguna, Tenerife, Spain*
[4]*Departamento de Astrofísica, Universidad de La Laguna, E-38205 La Laguna, Tenerife, Spain*

Accepted 2018 October 18. Received 2018 October 7; in original form 2018 July 28

ABSTRACT

The bulk of stars in galaxy clusters are confined within their constituent galaxies. Those stars do not trace the extended distribution of dark matter well as they are located in the central regions of the cluster's dark matter subhaloes. A small fraction of stars is expected, however, to follow the global dark matter shape of the cluster. These are the stars whose extended spatial distribution results from the merging activity of galaxies and form the intracluster light (ICL). In this work, we compare the bi-dimensional distribution of dark matter in massive galaxy clusters (as traced by gravitational lensing models) with the distribution of the ICL. To do that, we use the superb data from the Hubble Frontier Fields Initiative. Using the Modified Hausdorff distance (MHD) as a way of quantifying the similarities between the mass and ICL distributions, we find an excellent agreement (MHD $\sim$ 25 kpc) between the two components. This result shows that the ICL exquisitely follows the global dark matter distribution, providing an accurate luminous tracer of dark matter. This finding opens up the possibility of exploring the distribution of dark matter in galaxy clusters in detail using only deep imaging observations.

Key words: galaxies: evolution – galaxies: haloes – galaxies: photometry – dark matter.

1 INTRODUCTION

One of the first evidences of non-baryonic dark matter (DM) was found in galaxy clusters (Zwicky 1933, 1937). This collisionless DM makes up most of the mass in the Universe (Planck Collaboration XIII 2016), does not radiate and only interacts gravitationally with visible matter providing only indirect ways of detecting it. Since DM is an essential constituent of cosmological theories, its distribution within galaxy clusters would help us to distinguish not only among different scenarios on the nature of DM itself (i.e. warm versus cold particles; Primack & Blumenthal 1984), but also on different alternatives to DM as modified gravity (see e.g. Milgrom 2002; McGaugh 2015).

In this sense, gravitational lensing has proven to be an invaluable tool to study the DM distribution within clusters of galaxies (see for a review Kneib & Natarajan 2011; Hoekstra et al. 2013). Gravitational lensing helps us to understand structure formation, probes the nature of DM and fully captures the interplay between baryons and DM (e.g. Clowe, Gonzalez & Markevitch 2004; Markevitch et al. 2004). In particular, gravitational lensing offers a unique and powerful probe of the substructure of the DM in galaxy clusters, independently of the dynamical state of the object producing the lensing. Despite these great advantages, having access to the detailed mass distributions of the galaxy clusters through gravitational lensing is very demanding observationally. An accurate gravitational lensing reconstruction requires not only deep imaging to identify multiply lensed images but also long spectroscopic campaigns to confirm the redshift of these images. In this sense, finding an alternative observational proxy to trace the DM distribution in galaxies would be ideal.

X-rays might appear as a way to address this problem. Galaxy clusters emit in X-rays due to thermal bremsstrahlung produced in the highly ionized gas bound by the gravitational potential well of the cluster. This powerful emission is directly linked to the total gravitating mass they contain, such that they can be efficiently used as tracers of the cosmic distribution of mass within a considerable fraction of the observable Universe (e.g. Borgani & Guzzo 2001). While in more relaxed clusters it might be true that the X-rays follow the DM distribution, in galaxy clusters that are undergoing a merger process, the gas (dissipative) experiences ram pressure and is slowed, creating an offset between the DM and the X-ray emission. A well-known example of this is the Bullet Cluster (e.g. Clowe et al. 2004; Markevitch et al. 2004). For this reason, it is worth exploring an alternative luminous tracer for the detailed distribution of DM that improves the one provided by the X-ray maps, particu-

★ E-mail: mireia.montes.quiles@gmail.com

larly in those galaxy clusters that are not relaxed (i.e. the majority of cases).

In the current cosmological paradigm (ΛCDM), clusters of galaxies are assembled hierarchically by the accretion of galaxies or small galaxy groups. Observationally, one of the most revealing signatures of this assembly is the ICL (see Mihos 2016 for a review). This diffuse light is composed of a substantial fraction of stars, between 5 and 20 per cent of the total amount of stars in the cluster (e.g. Krick & Bernstein 2007; Burke, Hilton & Collins 2015; Jiménez-Teja et al. 2018; Montes & Trujillo 2018). The ICL forms primarily by the interaction and merging of satellite galaxies during the assembly of the cluster (e.g. Gregg & West 1998; Mihos et al. 2005; Montes & Trujillo 2014, 2018). The physical scales of the ICL, several hundreds of kpc, are similar to those of the DM distribution (e.g. Dubinski 1998), so it is reasonable to expect that this component will help us trace the global gravitational potential of its host cluster. In fact, Pillepich et al. (2014, 2018) used the Illustris and IllustrisTNG suites of simulations to explore stellar haloes in systems encompassing a wide range of masses. In their analysis, they found a correlation between the logarithmic slope of the stellar density profile at large radius[1] (i.e. in the region dominated by the stellar halo) and the total mass of the halo. Furthermore, they claimed that this slope can be as shallow as the underlying DM slope for masses as large as $M_h = 10^{14–15}$ $M_\odot$. That is, both stellar and DM haloes have similar shapes. This is a direct consequence of the hierarchical assembly of galaxy cluster. More massive haloes form later which means that they are less concentrated (e.g. Navarro, Frenk & White 1996, 1997; Gao et al. 2004). Consequently, if the host haloes are less concentrated a satellite infalling into the cluster gravitational potential deposit its stripped stars at large radius (see also Cooper et al. 2015). The Pillepich et al. (2014, 2018) prediction has been recently confirmed in Montes & Trujillo (2018, hereafter MT18). In such work, MT18 explore the correlation between the slope of the stellar density profile of the ICL and the total mass of the halo (M_{200}) in the Hubble Frontier Fields (HFF) clusters. They found that the slopes of the ICL of the HFF clusters follow the extrapolation of the theoretical expectations in Pillepich et al. (2018).

Motivated by the above result, we decided to take a step forward and explore whether the ICL can be used to trace in detail the DM distribution (including substructures) in galaxy clusters. In this work, we use the accurate mass maps built using gravitational lensing and compare those with the ICL bi-dimensional distribution. In order to do that, we use the exquisite data provided by the HFF Initiative (Lotz et al. 2017). The HFF Initiative appears as the perfect data set for exploring this as it not only provides the deepest images of six galaxy clusters ever observed with the *Hubble Space Telescope* (*HST*), but it also provides accurate gravitational lensing models of the clusters. The hundreds of multiply imaged background galaxies at different redshifts have allowed the construction of very accurate total mass maps of the clusters to an unprecedented spatial resolution (e.g. Jauzac et al. 2014, 2015b; Balestra et al. 2016; Diego et al. 2016a; Annunziatella et al. 2017; Williams, Sebesta & Liesenborgs 2018). These data not only provide a unique possibility to study the high-redshift Universe, but also substructure in galaxy clusters (e.g. Jauzac et al. 2016b).

[1]The radius used in Pillepich et al. (2018) to fit this slope of the density profile ranges between 30kpc $< R < R_{200c}$, with R_{200c} being the 3D virial radius.

Throughout this work, we adopt a standard cosmological model with the following parameters: $H_0 = 70\,\mathrm{km\ s^{-1}\ Mpc^{-1}}$, $\Omega_\mathrm{m} = 0.3$ and $\Omega_\Lambda = 0.7$.

2 DATA

In this section, we describe the observational data we have used to explore distribution of the ICL and the X-ray emission of the galaxy clusters. In addition, we describe the gravitational models used to characterize the distribution of total mass in the clusters.

2.1 *HST* near-IR data to characterize the ICL

The primary data set used for this work is based on the *HST* images of the six HFF clusters (ID13495, PI: J. Lotz, Lotz et al. 2017).[2] Details on the processing of the observational data from the six HFF clusters for the study of the ICL can be found in MT18 and are summarized below. As the ICL is more prominent at redder bands, in order to derive the bi-dimensional distribution of the ICL we used the *HST* *F*160*W* filter for each of the clusters.

The data were directly retrieved from the HFF webpage.[3] For the ACS/WFC (Advanced Camera for Surveys Wide Field Camera; Ford et al. 1998) and WFC3 (Wide Field Camera 3; MacKenty et al. 2008) cameras, flat-fields are claimed to be accurate to better than 1 per cent across the detector. The *F*160*W* images used here are drizzled science images with pixel size 0.″06 (the native WFC3 pixel is closer to twice this value: 0.″13). The sky correction was carefully done by subtracting a constant measured in ∼30 apertures of $r = 25$ pix (1.″5), well separated from any sources or diffuse light to minimize contamination. Kolmogorov–Smirnov tests were performed to confirm that the measured background followed a Gaussian distribution, with p-values >0.05.

Once the images are corrected for sky background, the next task is to identify the ICL on the images. This is a highly non-trivial step as it requires to mask all the foreground and background objects on the images which are not part of the cluster and also all the cluster galaxies that are not the brightest cluster galaxy (BCG). Observations (e.g. Krick & Bernstein 2007) have shown that the ICL is more centrally concentrated than the galaxies of the cluster implying that this light is formed via the mergers that build up the BCG. Consequently, there is no clear differentiation between the outskirts of the BCG and the extended ICL (see Mihos 2016). Therefore, we did not attempt to separate both components. Even though in MT18 we performed extensive masking of sources that are not the BCG and ICL, for this work we further increased the masks to get rid of any remaining low surface brightness light in the periphery of the galaxies that might contaminate the ICL.

A further complication in the analysis of the ICL distribution is that the HFF clusters are in the process or have experienced recent merging (Lotz et al. 2017). Consequently, identifying the BCG is a not straightforward task and in three of the galaxy clusters (A2744, M0416, and A370) we decided to label the two most massive galaxies as BCGs. In these three cases, we effectively have two centres for the ICL distribution. Finally, in order to reduce the noise, especially at larger distances from the BCG(s), we smoothed the background-subtracted images using a Gaussian of $\sigma = 15$ pix (∼0.″9).

[2]http://www.stsci.edu/hst/campaigns/frontier-fields/FF-Data
[3]http://www.stsci.edu/hst/campaigns/frontier-fields/FF-Data

Table 1. Summary of the ACIS observations from the *Chandra* telescope used to derive the bi-dimensional X-ray distributions.

Cluster	Obs. ID	PI	Exp. Time (ks)
Abell 2744 (A2744)	8477	Kempner	45.89
MACS J0416.1-2403 (M0416)	17313	Jones	71.13
MACS J0717.5+3745 (M0717)	16305	Murray	94.34
MACS J1149.5+2223 (M1149)	16306	Murray	79.71
Abell S1063 (AS1063)	18611	Kraft	49.46
Abell 370 (A370)	515	Garmire	88.03

2.2 X-rays imaging

In order to compare the shapes of the X-ray emission of the cluster to the mass distributions, we retrieved Advanced CCD Imaging Spectrometer (ACIS) images from the *Chandra* Data Archive.[4] The spatial resolution for *Chandra* ACIS imaging is ∼1 arcsec. The images were downloaded already processed. The clusters were observed with ACIS-S in 'VFAINT' mode, except for A370 which was observed by ACIS-I in 'FAINT' mode. They were processed with CXC software using CalDB. The versions of the CXC software used for processing the X-rays images are: A2744: 8.4.4, M0416: 10.3, M0717: 10.1.1, M1149: 10.2.1, AS1063: 10.5, and A370: 8.1.1. For CalDB the versions used are: A2744: 4.4.9, M0416: 4.6.4, M0717: 4.6.4, M1149: 4.6.4, AS1063: 4.7.2, and A370:4.1.4a.

A summary of the *Chandra* data used in this work including observation ID numbers, principal investigator (PI), and effective exposure times can be found in Table 1.

2.3 Mass models based on gravitational lensing

The primary science goal of the HFF is to use the clusters as gravitational lenses to push the limits of current observations and study the faintest and most distant galaxies (Lotz et al. 2017). However, in order to interpret many of the properties of those lensed galaxies, reliable models of the distribution of the mass for each cluster are required. As part of the HFF Initiative, different lensing models of the mass distribution for each of the six clusters have been provided to facilitate the analysis of the data. Having access to deep observations and hundreds of background sources at different redshifts, they provide very accurate (0.2–11 per cent, Lotz et al. 2017) maps of the mass distribution of the clusters.

Cluster mass estimates determined by lensing are valuable because the method requires no assumption about the dynamical state or formation history of the cluster and also provides us with an independently measured shape of the underlying DM halo.

To conduct our goals, we used the κ maps defined in units of the lensing critical density at the redshift of the lens ($\kappa = \Sigma/\Sigma_{\rm crit}$) defined by

$$\Sigma_{\rm crit} = \frac{c}{4\pi G}\frac{D_S}{D_L D_{LS}} \quad (1)$$

using the angular-diameter distances from observer to source D_S, observer to lens D_L and lens to source D_{LS}.[5] The models are scaled to $D_{LS}/D_S = 1$. The lensing models are retrieved from MAST[6] and summarized in Table 2. We therefore made use of the *kappa* maps from all the available models including CATS (Jullo & Kneib 2009; Richard et al. 2014; Jauzac et al. 2015a,b, 2016a; Limousin et al. 2016; Lagattuta et al. 2017; Mahler et al. 2018), Diego (Lam et al. 2014; Diego et al. 2015a,b, 2016a,b, 2018), GLAFIC (Oguri 2010; Ishigaki et al. 2015; Kawamata et al. 2016, 2018), Keeton (Keeton 2010), Merten (Merten et al. 2009, 2011), Sharon/Johnson (Johnson et al. 2014), Williams/GRALE (Liesenborgs, De Rijcke & Dejonghe 2006; Grillo et al. 2015; Sebesta et al. 2016), BradaŽc (Bradač et al. 2009; Hoag et al. 2016), Zitrin-NFW (Zitrin et al. 2013, 2015), Zitrin-LTM (Zitrin et al. 2012, 2015), and Caminha et al. (2017).

[4] http://cda.harvard.edu/chaser/

[5] http://archive.stsci.edu/prepds/frontier/lensmodels/webtool/hlsp_frontier_model_lensing_primer.pdf

[6] https://archive.stsci.edu/prepds/frontier/lensmodels/

3 2D SHAPE MATCHING

The aim of this work is to study how well the distribution of the diffuse ICL in clusters traces the underlying distribution of the total mass of the cluster (baryonic + DM). In order to do that, we have taken advantage of the gravitational lensing (κ maps) models as a way to infer the 'true' distribution of mass in the cluster. The question now is how to quantify the similarity between the bi-dimensional distribution of the ICL in comparison with the mass maps derived from gravitational lensing. In this work, we follow a two steps approach. First, we visually explore whether the mass distribution and the ICL have the same form by exploring the shape of the isophote and isomass contours of both distributions. In a second step, we quantify the similarities between both distributions through the Modified Hausdorff distance.

3.1 Contours

To explore whether the ICL follows the 2D distribution of DM in the HFF clusters, we derived the isocontours for each of the different components we are studying: light (ICL) and mass. In addition, to compare with the hot gas component, we also extract the isocontours for the X-ray emission. In order to have a sensible comparison, the isocontours of each map were obtained at the same physical radial distances: 50, 75, 100, 125, and 140 kpc. To measure a radial distance, we need to define a centre. Because the location of the centre affects the location of the different radial distances, and therefore the shape of the contours, we expand on the choice of centres for each component.

In the case of the ICL, the obvious centre is the one provided by the position of the BCG (or BCGs). For the gravitational lensing mass models, we also use the peak(s) of the distribution of total mass (which roughly corresponds to the position of the BCG(s) in each cluster). In the case of the X-ray observations, the centre is the location of the peak of emission. This is done for a reason: the gas is a dissipative component and its distribution is clearly disturbed in the majority of the HFF clusters. Therefore, the choice of the peak of X-rays as the centre of the hot gas distribution has the aim of making a much fairer comparison in the disturbed cases. Nevertheless, we also tested our procedure by fixing the centre of the different distributions to the BCG(s) and the qualitative results of this paper do not change with the choice of the centres.

Once the centres are chosen, we obtain the radial light/mass profiles of the ICL, X-ray emission, and mass maps. To that end, we average the intensities in 16 logarithmic spaced bins from 0 to 200 kpc from the BCG(s). The radial distance to each pixel on the images is computed as the elliptical distance to its nearest centre (BCG) as seen in the left-hand panel of Fig. 1. The morphological parameters (i.e. axial ratio and position angle) for these galaxies are

Table 2. Summary of the gravitational lensing models used.

Cluster	Models				
A2744	CATS v4.1	Diego v4.1	GLAFIC v4	Keeton v4	Merten v1
	Sharon & Johnson v4	Willians v4	Bradač v2	Zitrin-NFW v3	Zitrin-LTM v1
M0416	CATS v4.1	Diego v4.1	GLAFIC v4	Keeton v4	Merten v1
	Sharon & Johnson v4	Willians v4	Bradač v3	Zitrin-NFW v3	Zitrin-LTM v1
	Caminha v4				
M0717	CATS v4.1	Diego v4.1	GLAFIC v3	Keeton v4	Merten v1
	Sharon & Johnson v4	Willians v4	Bradač v1	Zitrin-LTM v1	
M1149	CATS v4.1	Diego v4.1	GLAFIC v3	Keeton v4	Merten v1
	Sharon & Johnson v4	Willians v4	Bradač v1	Zitrin-LTM v1	
AS1063	CATS v4.1	Diego v4.1	GLAFIC v4	Keeton v4	Merten v1
	Sharon & Johnson v4	Willians v4.1	Bradač v1	Zitrin-NFW v1	Zitrin-LTM v1
A370	CATS v4	Diego v4.1	GLAFIC v4	Keeton v4	Merten v1
	Sharon & Johnson v4	Willians v4.1	Bradač v1	Zitrin-NFW v1	Zitrin-LTM v1

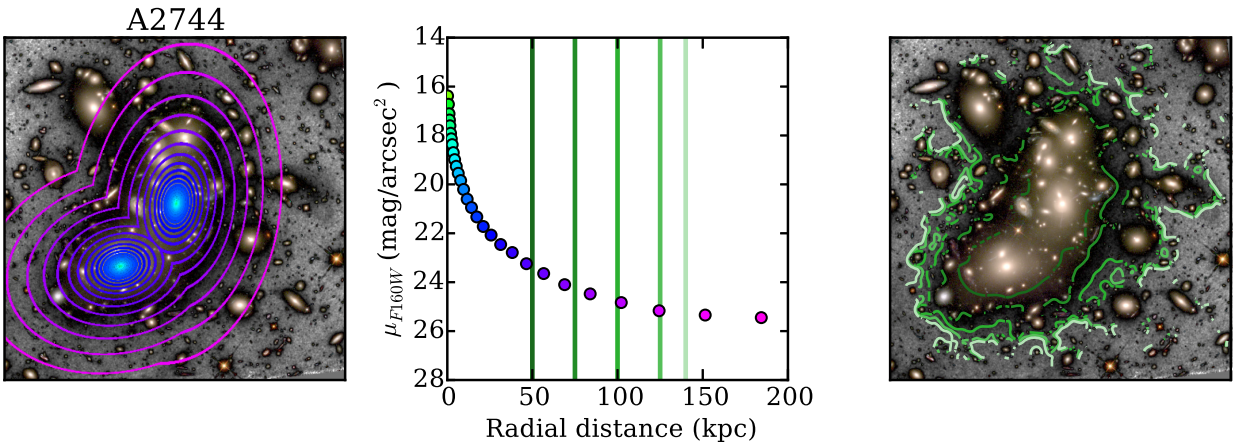

Figure 1. A description of the procedure for obtaining the isocontours of ICL, mass, and X-rays. *Left-hand panel:* RGB image of one of the HFF clusters with the different spatial regions in which the surface brightness profile is measured. The radial distance to each pixel in each radial bin is computed as the elliptical distance to its nearest BCG. *Middle panel: F*160*W* surface brightness profile of the cluster averaging the values in each radial bin. The green vertical lines correspond to the radial distances of 50, 75, 100, 125, and 140 kpc where we infer the values to draw the contours. *Right-hand panel:* contours of equal surface brightness for the values obtained at the radial distances indicated in the middle panel.

given by `SExtractor` (see MT18 for further details). This procedure is illustrated in Fig. 1 for the ICL. Using this radial profile, we interpolated the intensities of the ICL/mass/X-ray profiles at the radial distances 50, 75, 100, 125, and 140 kpc. Once the intensities at different radial distances are characterized, we build the contours on the different maps that correspond to such intensities using the function `contour` in `matplotlib`. The `contour` function provides and draws isocontour lines at different given values of the image, in this case the intensities for the five radial distances. The contours for the five distances for each cluster and each component are shown in Fig. 2. Left-hand panels show the contours for the ICL (green), middle panels for the total mass of the cluster (blue) and right-hand panels for the X-ray emission (red). To make a proper comparison of the contours, we have applied the same masking that we derive in the *F*160*W* filter to the rest of the maps.

The mass models shown in the middle panels of Fig. 2 are the models representative of the average shape of all the models at all radius for each cluster (i.e. the mass models used are: A2744: GLAFIC v4, M0416: Sharon & Johnson v4, M0717: CATS v4.1, M1149: CATS v4.1, AS1063: Diego v4.1, A370: Keeton v4).

For ease of comparison, we plotted in Fig. 3 the contours of the ICL (green), mass (blue), and X-rays (red) corresponding to a radial distance of 125 kpc. The underlying image is a composite of an RGB colour image created using the *F*606*W*, *F*814*W*, and *F*125*W* filters and a black and white *F*160*W* image for the background.

A first visual inspection shows that the bi-dimensional distribution of the ICL is comparable to the mass distribution of the clusters. However, this is not always the case for the X-rays. Only in one of the six cases, A370, the X-ray distribution is in agreement with the total mass distribution and, also, the ICL. This observed difference between the X-ray emission and the distribution of total mass is expected. The HFF clusters are undergoing or have undergone recent mergers. In these cases, the hot gas that produces the X-ray emission experiences ram pressure and is slowed creating an offset between the DM and the X-ray emission. As mentioned in the Introduction, a well-known example of this is the Bullet Cluster where the X-ray and DM distributions are different (Clowe et al. 2004; Markevitch et al. 2004).

3.2 Modified Hausdorff Distance

Admittedly, a visual inspection is not an ideal quantifier of the resemblance amongst the three sets of data. In order to measure the similarities between the contours of the different maps of the

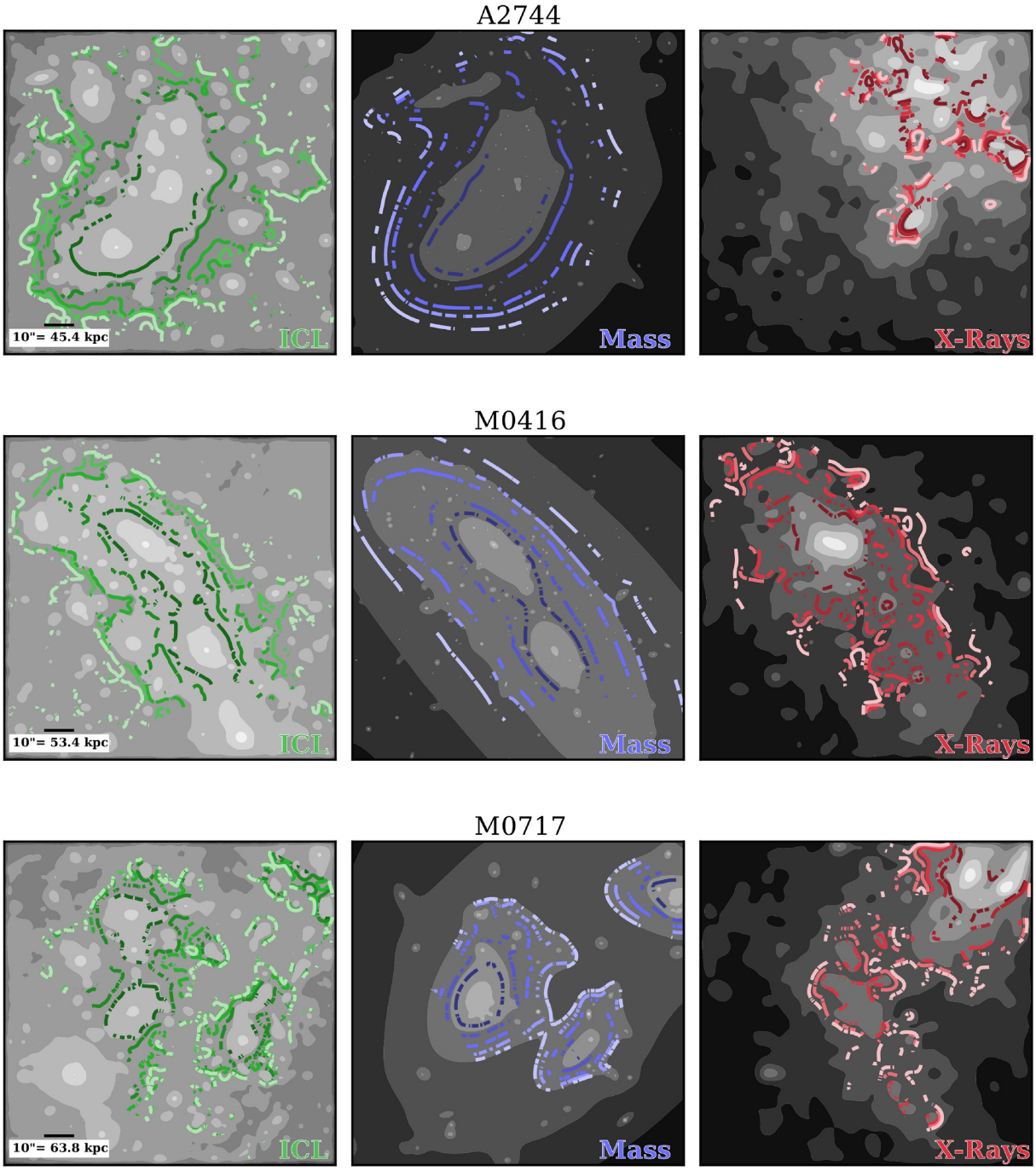

Figure 2. Comparison of the distribution of the ICL from the *F*160*W* images (left-hand panels, green), the mass distribution of the cluster based on its gravitational lensing (middle panels, blue), and the distribution of the hot gas X-ray emission (right-hand panels, red) for each of the FF clusters. The size of the FOV is 110 × 110 arcsec^2 in each cluster. We overplotted the contours for five different distances: 50 (darkest colours), 75, 100, 125, and 140 (lightest colours) kpc.

clusters, we chose a metric used in shape matching: the Modified Hausdorff distance (MHD). The MHD is a measure of how far two subsets are from each other. Given two sets of a metric space, the Hausdorff distance (HD), named after Felix Hausdorff, is defined as the maximum distance of all the distances from a point in one set to the closest point in the other set. For two sets on points $X = \{x_1, x_2, \cdots x_{N_x}\}$ and $Y = \{y_1, y_2, \cdots y_{N_y}\}$, the HD is

$$HD(X, Y) = max(d(X, Y), d(Y, X)) \quad (2)$$

$$d(X, Y) = \max_{x_i \in X} \min_{y_j \in Y} ||x_i - y_j||. \quad (3)$$

The smaller the value of HD, the more similar the two point sets are. Therefore, this distance has applications in the context of shape matching (Huttenlocher, Klanderman & Rucklidge 1993). However, as the Hausdorff distance is set by the maximum distance among two sets of points it can be very sensitive to outliers even when the objects are fairly similar (e.g. Dubuisson & Jain 1994). For that reason, Dubuisson & Jain (1994) introduced the MHD (see

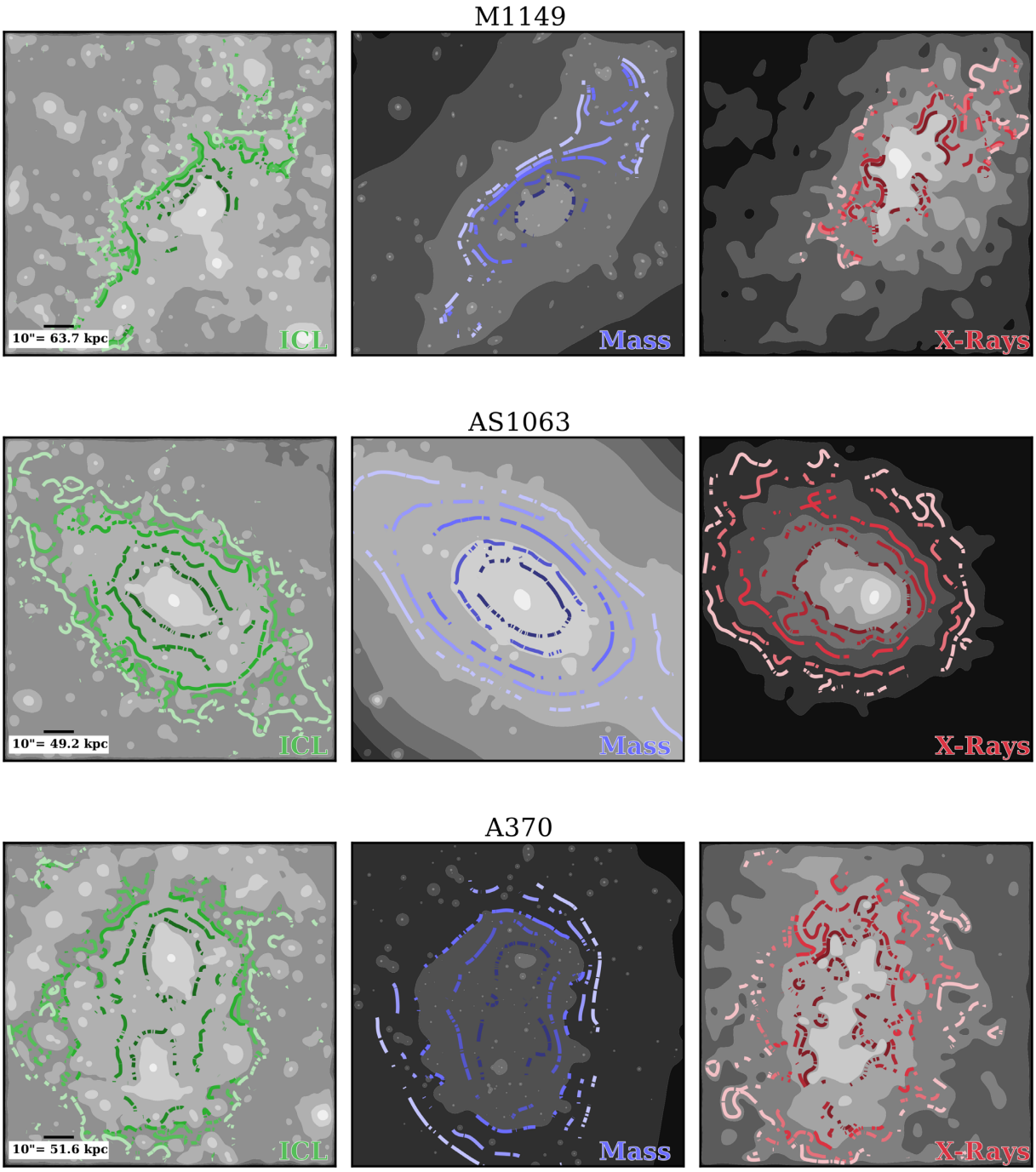

Figure 2. – *continued*

also Huttenlocher et al. 1993). The MHD changes equation (3) for

$$d(X, Y) = \frac{1}{N_X} \sum_{x_i \in X} \min_{y_j \in Y} ||x_i - y_j||, \quad (4)$$

where N_X is the number of elements in the set of points X. The MHD is more robust to outliers than the original HD form. Another interesting property of the MHD is that its value increases monotonically as the difference between the two sets of points increases.

We can interpret the MHD as the mean distance difference between two sets of data. In our case we are interested in exploring how well a given tracer (X-ray or ICL) follows the distribution of the total mass of the cluster. Consequently, the MHD will give us the mean difference in distance (in kpc) between the tracer and the mass model. For instance, an MHD value around 20 kpc would mean that the average departure of the ICL contours from the mass contours is of the order of the size of the Milky Way (Goodwin, Gribbin & Hendry 1998).

4 RESULTS

In Fig. 4, we plotted the MHD between the ICL and the mass maps as a function of the radial distance for each of the HFF clusters. The

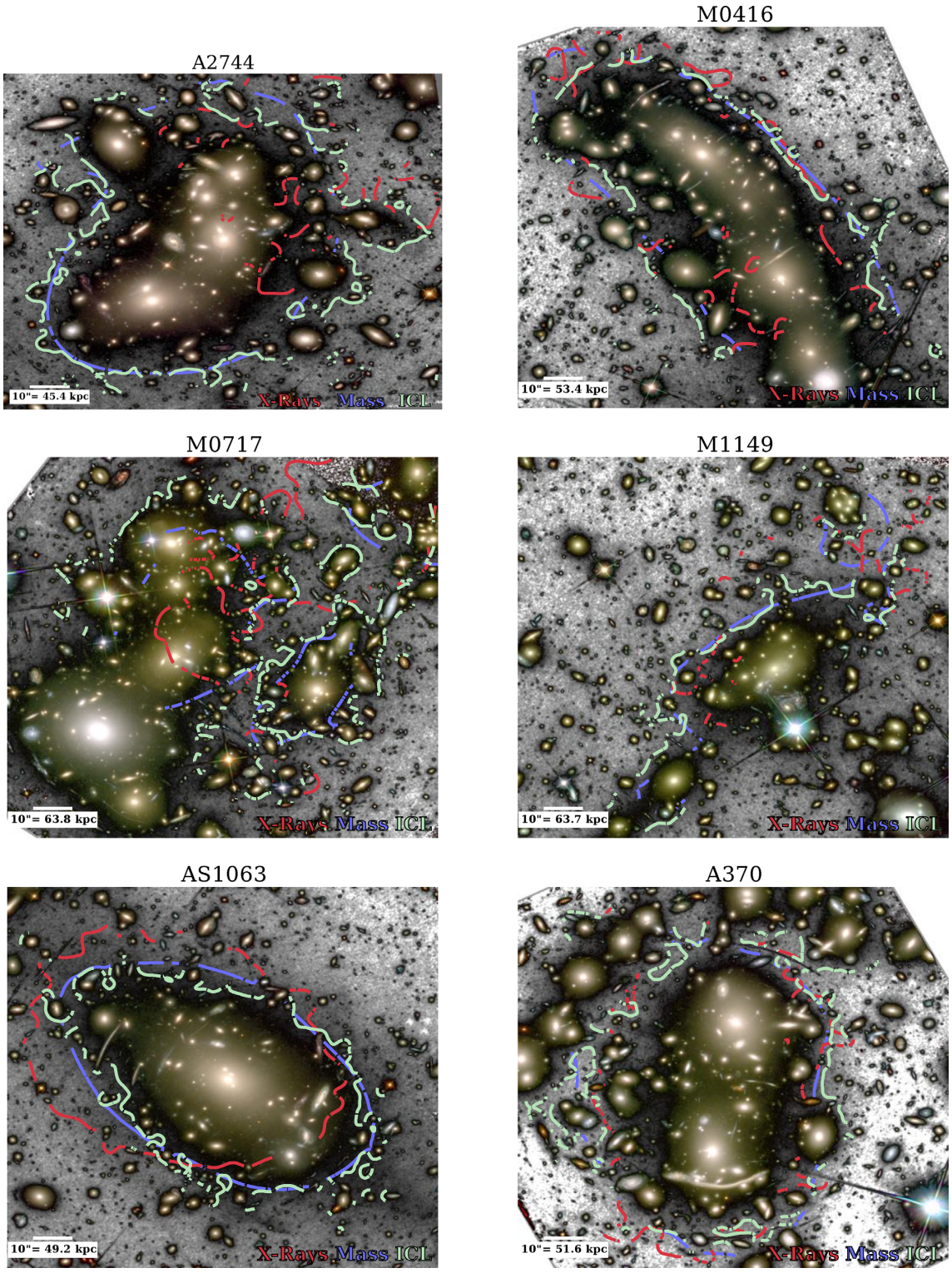

Figure 3. RGB images of the HFF clusters with the contours of ICL (green), X-rays (red), and Mass (blue) at a radial distance of 125 kpc overplotted. The RGB images are a combination of the *F*606*W*, *F*814*W*, and *F*125*W* bands, whereas a black and white *F*160*W* image is used for the background.

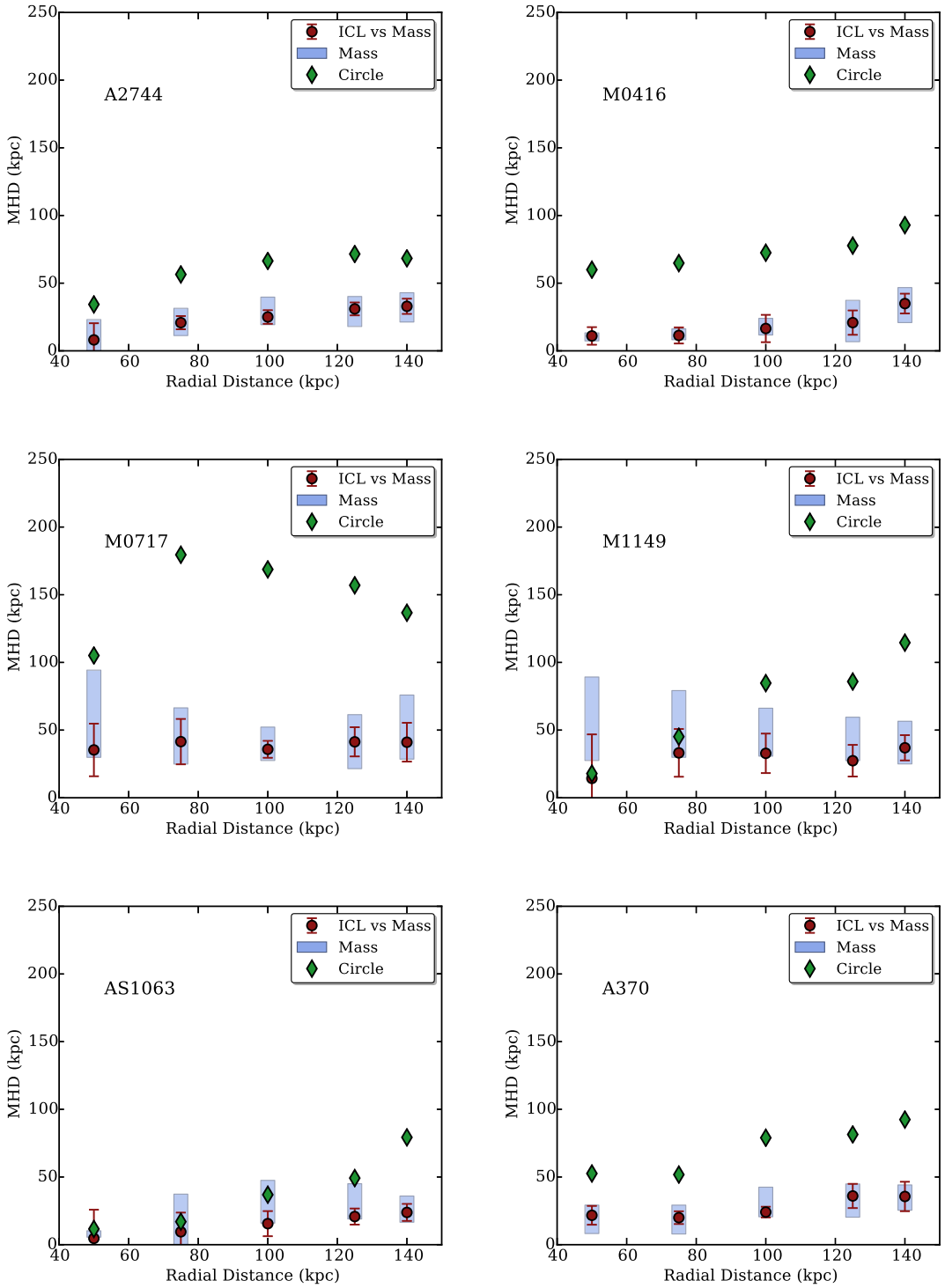

Figure 4. Modified Hausdorff Distance (MHD) between the ICL of the HFF clusters and the different mass models from gravitational lensing. The blue rectangles enclose the 68 per cent of the measured MHDs among the mass models themselves. The red filled circles represent the median values of the MHD of the ICL when compared with all the mass models. As a visual guide, we have also plotted the value of the MHD when comparing the ICL contour with a circle at each given radius (green diamonds). The departure of the diamonds from the red circles indicates an increasing ellipticity of the ICL distribution.

red circles represent the median[7] value of the MHD at each distance resulting from the comparison between the contours of the ICL and the different mass maps for each of the models listed in Table 2. The error bars represent the 1σ scatter. The median values and errors are given in Table A1. The process of converting the lensing constraints into matter distribution is not unique, and therefore different models use different methodologies and also other tracers of the

[7]We use the resistant median i.e. trimming away the 5σ outliers.

gravitational potential of the cluster to constrain the degeneracies (X-rays, galaxy kinematics, etc., see Meneghetti et al. 2017 for a review of the different methodologies). Priewe et al. (2017) showed that the magnification maps based on different lens inversion techniques differ from each other by more than their statistical errors due to degeneracies. This difference can be understood as the intrinsic uncertainty in the mass distributions of the clusters. Accordingly, in order to evaluate how reasonable is the similarity among the ICL and the mass models, it is necessary to quantify what is the typical MHD between the different mass models themselves for a given cluster. The blue rectangles in Fig. 4 represent the 1σ uncertainty of the MHD among the mass models (enclosing 68 per cent of them[8]). The median values and uncertainties among the different mass models are given in Table A2.

In those cases where the MHD between the ICL and the mass models is similar to the typical MHD among the different mass models implies that the ICL is basically identical in shape to the isomass contours provided by the different mass models. In other words, the ICL distribution is fully compatible (within the uncertainties) with the mass distributions of the lensing models. In all the cases, there is an excellent agreement between the ICL distribution and the distribution of total mass. The average MHD between the ICL and the mass models and the mass models themselves is around 25 kpc for most of the clusters. This means that the average difference between the contours is around the size of a Milky Way like galaxy. It is noteworthy that the two higher redshift clusters, M0717 and M1149, exhibit larger uncertainties and higher MHD ($\sim$50 kpc) at all radii. This is caused by a lack of spectroscopically confirmed lensed systems and images, and therefore less constrained mass models (e.g. Jauzac et al. 2016a; Limousin et al. 2016; Natarajan et al. 2017; Williams et al. 2018). In the following, we will discuss in more detail each cluster.

A2744 A2744 is the closest of the HFF clusters at $z = 0.308$. It shows a significant degree of substructure (Jauzac et al. 2016b) and it is highly disturbed (Merten et al. 2011; Owers et al. 2011) undergoing a merger. Consequently, it is not surprising that the distribution of X-rays does not follow the mass distribution. However, we find a nice agreement between the ICL and the mass models. All this is quantified in the upper left panel of Figs 4 and 5. Fig. 4 shows a median MHD between the ICL and the different mass model of 25 kpc, compatible with the uncertainties among the different models (blue rectangles). Fig. 5 shows that this agreement does not hold in the case of the distribution of X-rays. In fact, the average MHD between the X-ray distribution and the mass models is around 110 kpc. This is consistent with Owers et al. (2011), who found that there is no corresponding galaxy overdensity to the peak of the X-ray emission which interpreted as the stripped atmospheres of the merging subclusters.

M0416 M0416 is an elongated cluster at $z = 0.397$ clearly undergoing a merging event as is shown by its X-ray morphology (Mann & Ebeling 2012). Fig. 4 shows that the radial median value of the MHD between the ICL and the mass distribution is comparable to the uncertainties derived from the models, i.e. we find a good agreement between ICL and mass with a mean MHD of 17 kpc. In the case of the X-rays, Fig. 5 shows that while the difference is not as big as in the case of A2744, the X-ray distribution is still not as good tracer of the mass distribution of this cluster as the ICL. For the X-rays, the mean MHD is 28 kpc.

M0717 this cluster is the farthest ($z = 0.545$, Edge et al. 2003), one of the most massive and the strongest lenser of all the clusters in the HFF sample (Lotz et al. 2017). This is a highly disturbed massive cluster (Ebeling et al. 2007) with a complex structure and an ongoing merger (Ma, Ebeling & Barrett 2009) as shown by significant offsets between the X-ray emission and the mass distribution (van Weeren et al. 2017). In Fig. 4, we find a good agreement between the ICL and the total mass distribution. However, contrary to what we can infer from Figs 2 and 3, the agreement at $>$100 kpc between X-rays and the distribution of mass in Fig. 5 is not seen in the contours. This might be caused by the presence of a peculiarity that it is not seen in the other clusters (see Fig. 2). In the inner 110×110 arcsec^2 of this cluster, there are three different separate substructures. That creates three separate sets of contours for the ICL and the mass models. Moreover, the X-rays also present separate contours. For the future, it would be worth exploring whether the MHD might be able to properly deal with comparing complex shapes.

M1149 a cluster at $z = 0.543$, M1149 is an X-ray-elongated cluster with a complex merger history (Kartaltepe et al. 2008; Zitrin & Broadhurst 2009; Lotz et al. 2017). As mentioned in MT18, this cluster presents two bright stars and a foreground galaxy in the lower right part of the images. To prevent contamination on the ICL stellar populations, and to a lesser extent the shape of the ICL, we masked part of the image. That causes that in Fig. 2 only the half left part of the contours are shown. As we mentioned before, mass models in this cluster have a larger MHD due to the small number of multiple-imaged systems. This causes that the image positions predicted by the best-fitting models are less precise than in other clusters (Jauzac et al. 2016a). The X-rays present an offset with respect to the ICL and the models, shown by the respective values of MHD in Fig. 5. The mean MHD for the ICL is 33 kpc, while for X-rays is 60 kpc.

AS1063 AS1063 is a cluster at $z = 0.346$. Even though it is the most relaxed in the HFF sample (Diego et al. 2016b), it exhibits asymmetry in its X-ray emission map (Fig. 2) suggesting a recent ($\sim$0.75 Gyr) 1:4 mass ratio merger (Gómez et al. 2012). The ICL traces the mass distribution of the cluster with a mean MHD of 16 kpc as seen in Fig. 4. The asymmetry of the X-rays with respect to the mass distribution and the ICL is shown in Fig. 5. As expected, the X-rays have a mean MHD larger than for the ICL: 34 kpc.

A370 A370 is one of the best-studied strong-lensing clusters, $z = 0.375$, as it is the host of the first observed Einstein ring (Paczynski 1987; Soucail et al. 1987). Richard et al. (2010) found that this cluster is likely the recent merger of two subclusters of equal mass based on small offsets among X-rays, mass and stellar light (although no offset is present in Lagattuta et al. 2017). Fig. 2 shows the resemblance among the shape for the three tracers. The value for the mean MHD of the ICL is 24 kpc (Fig. 4). However, contrary to the other clusters, the X-rays in this cluster match very closely the 2D distribution of the ICL and therefore of the total mass of the cluster. The mean value for the MHD of the X-rays is 25 kpc.

[8]Note that the middle panel of Fig. 2 shows the gravitational lensing model with the MHD closer to the median MHD computed among models at all radii.

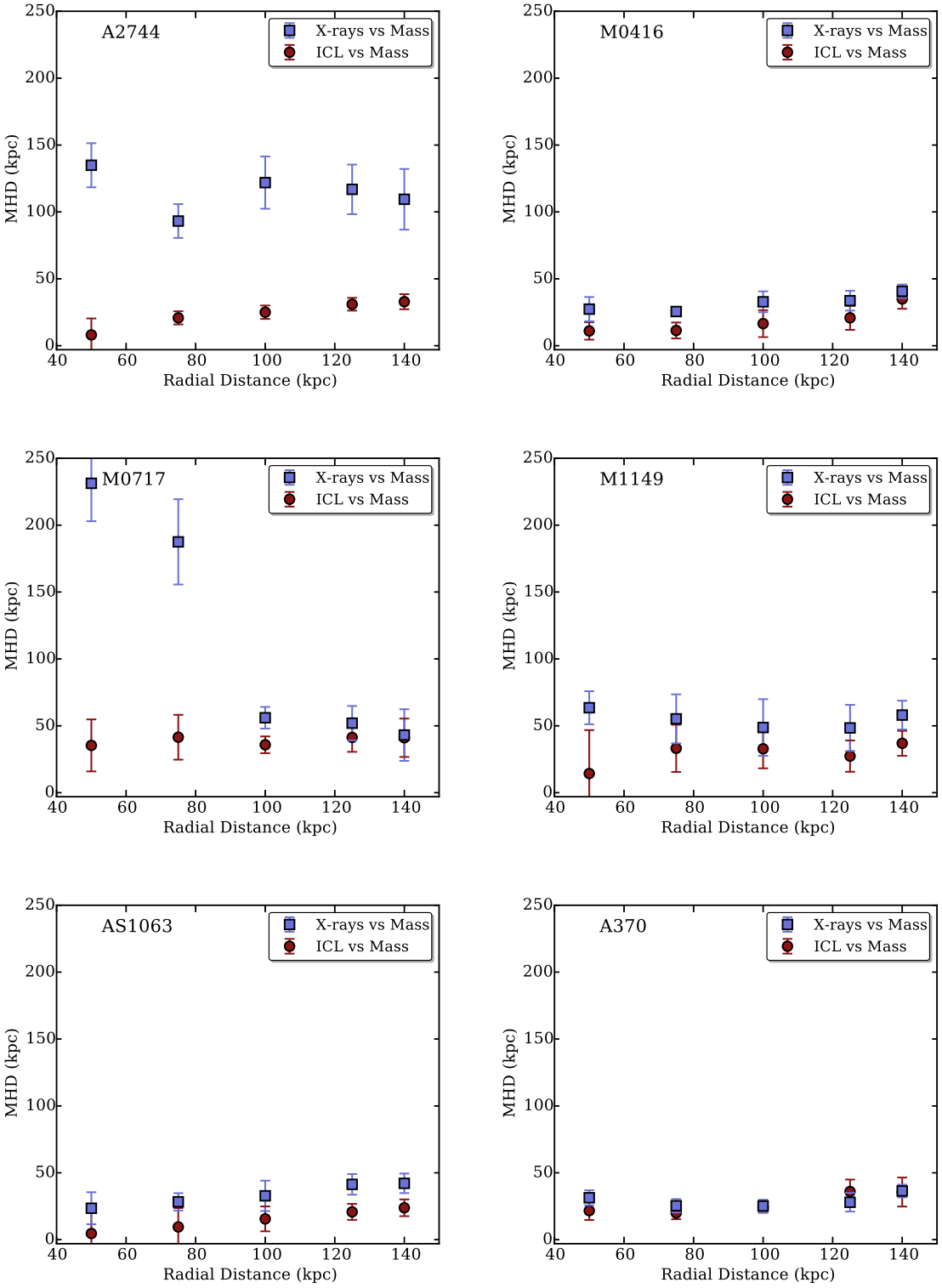

Figure 5. Comparison between the MHD obtained by comparing the distribution of ICL with the mass models (red filled circles) and that comparing the X-rays distribution with the mass models (blue filled squares). In most of the cases, except A370, the X-rays distribution as compared with the underlying distribution of total mass has a large MHD, thus proving the power of the ICL as a tracer of dark matter halos.

5 DISCUSSION

The results presented in this work demonstrate the extraordinary power of the ICL to trace the shape of the total mass of the galaxy clusters. The depth, the multiwavelength coverage, and the wealth of ancillary data available for the HFF clusters make possible to have accurate total mass distributions from gravitational lensing, and therefore, to explore how well the ICL follows mass.

5.1 Is the X-ray emission a good tracer of the distribution of the total mass?

The hot gas distribution, as traced by the X-ray emission maps, has been extensively used in the past as a luminous tracer for the total mass of the clusters (e.g. Borgani & Guzzo 2001). In this work, we have explored whether the ICL is a better and more detailed representation of the detailed distribution of the total mass in clusters than the hot gas. In most of the cases, there is no similarity between the mass distribution and the X-ray emission. This is not surprising as the HFF clusters are all in the process or have experienced a recent merger. While in more relaxed clusters it might be true that the X-rays follow the DM distribution, in interactions, the gas (dissipative) experiences ram pressure and is slowed, creating an offset between the DM and the X-ray emission. However, one of the HFF clusters (although it is currently undergoing a merging process) does exhibit a good correspondence among ICL, X-rays, and mass: A370. In Richard et al. (2010), the authors suggested that this agreement is the consequence of the two subcomponents of the cluster having a large projected velocity along the line of sight, which will explain the small offset seen between the X-rays and the DM peaks (see also Lagattuta et al. 2017).

Based on our quantitative analysis using the MHD, we conclude that the distribution of the ICL is a much better luminous tracer of the distribution of the total mass of the clusters than the X-ray emission. This is a significant step forward on our understanding of how the mass is located in these large-scale structures. Having an accurate luminous signature for the total mass of the clusters will allow to make a detailed comparison with the dark matter distribution predicted by cosmological simulations.

5.2 How accurate is the ICL as a tracer of the mass distribution of the cluster?

5.2.1 The accuracy of the mass models

Despite the exquisite quality of the HFF data, the limited information given by the finite number of constraints (the multiple lensed images) produces a certain degeneracy in recovering the mass distribution maps. The intrinsic statistical errors of the HFF mass models (the rms between the predicted image position and the observation) are $\lesssim$1.4 arcsec (e.g. Jauzac et al. 2015a; Zitrin et al. 2015; Lagattuta et al. 2017; Meneghetti et al. 2017; Remolina González, Sharon & Mahler 2018) which translates to distances of $\lesssim$6 ($\lesssim$9) kpc at redshift $z = 0.3$ ($z = 0.5$). This is less than the typical MHD that we found between the ICL (i.e. $\sim$25 kpc) and the mass models. However, these statistical errors of the models are not a good representation of the real uncertainties at recovering the underlying mass distribution. In fact, the multiple lensed images of a given cluster can be reproduced by different mass distributions hence a better description of the systematic uncertainties is provided by the dispersion of the mass models. We have characterized such uncertainty by the range of MHDs among the different mass models (blue rectangles in Fig. 4). We found that the similarity between the total mass distribution and the ICL is within these systematic errors (see Fig. 4). In this sense, with our current capabilities to characterize the mass distribution of the clusters, the ICL perfectly describes how the mass is distributed.

5.2.2 Why the ICL traces the underlying mass distribution?

In this paper, we have shown that with the current level of precision at building mass models for galaxy clusters, the distribution of the ICL describes how the mass is distributed. A natural question then is why the ICL is such an accurate tracer of the underlying mass distribution? The answer to this is connected with the origin of the ICL. The ICL is the product of the stripping of galaxies as they fall into the cluster. Those stripped stars are not bound to any particular galaxy but to the cluster itself. Furthermore, both the ICL and the DM act as collisionless components following the same gravitational potential. On the contrary, X-ray emitting gas is highly collisional, and consequently, its dynamic and spatial distribution does not follow the same rules as the collisionless components.

In order to explore how well the stellar haloes trace their DM haloes, Pillepich et al. (2018) analysed a sample of 4000 galaxies in the IllustrisTNG simulation. Taking advantage of the large cosmological volume of the simulation (reaching $\sim 300^3$ Mpc^3), they explored a wide range of halo masses from $\sim 1 \times 10^{12}$ to 5×10^{14} M$_\odot$. They found a correlation between the slope of the density profile of the stellar halo and the total mass of the system. These can be interpreted as a signature of the hierarchical assembly of haloes in the ΛCDM paradigm. More massive haloes form later which means that they are less concentrated (e.g. Navarro et al. 1996, 1997; Gao et al. 2004). These haloes also tend to accrete more and more luminous satellites (e.g. Gao et al. 2004) at recent times. Those satellites tend to have larger apocentres and deposit their stars at large radii ($\sim$100 kpc, Cooper et al. 2015) forming a less centrally concentrated stellar profile.

The correlation between the slope of the density profile of the stellar halo and the total mass of the systems was already explored in MT18. We found that this relationship holds even at masses as large as the masses of the haloes of the HFF clusters ($\sim 3 \times 10^{15}$ M$_\odot$). Furthermore, Pillepich et al. (2018) found that the stellar halo of the clusters could be as shallow as their dark matter halo. Inspired by this, in this paper we have shown that it is not only the global (1D) profile distribution of the ICL which agrees with the general slope of the dark matter halo but also its bi-dimensional structure.

The findings of this paper have an extraordinary consequence: the ICL is a powerful tool to study DM haloes in large structures. Using this diffuse light has more advantages than other tracers of the gravitational potential of the cluster, e.g. X-rays. In fact, the observation of the ICL, although challenging, is less time consuming than other observables. For example, gravitational lensing requires not only deep images to identify the multiply lensed images but also spectroscopy to confirm their redshifts. In comparison, for observing the ICL only deep imaging observations are required. Needless to say that, compared with X-ray data, the resolution achievable with optical data is better, allowing also to trace substructure at higher redshifts. On top of that, the HFF images target the centres of the clusters, where other phenomena (not necessarily related to the mass distribution) can contribute to the X-ray emission (e.g. active galactic nucleus).

6 CONCLUSIONS

The results presented in this work demonstrate the extraordinary power of the ICL to trace the detailed shape of the underlying dark matter halo of galaxy clusters. Taking advantage of the superb data and the mass models from gravitational lensing provided by the HFF Initiative, we quantified the similarity between the total mass of the clusters and the ICL. To do that, we adopted a metric used in object shape matching: the Modified Hausdorff distance. The MHD gives us the mean spatial difference (in kpc) between the bi-dimensional distributions of the total mass of the cluster and its ICL. We find the following:

(i) The mean MHD difference between the total mass distribution and the ICL is ∼25 kpc. This difference is similar to the typical difference among the different techniques of lens inversion to reconstruct the total mass maps.

(ii) In most of the cases, the X-rays are not tracing well the distribution of the total mass of the cluster, as the hot gas is easily perturbed in merging clusters. The ICL is shown to be a much better tracer of the mass distribution than the hot gas.

In summary, the study of the spatial distribution of the ICL stands out as a promising way to infer, in high detail, the properties of the underlying DM haloes in galaxy clusters. A great advantage of the ICL is that it can be observable from ground-based telescopes too (e.g. Mihos et al. 2005; Krick & Bernstein 2007; Iodice et al. 2017), where specially dedicated low surface brightness observations (e.g. Duc et al. 2015; Trujillo & Fliri 2016; Huang et al. 2018) will minimize observational biases.

The next step will be to extend this analysis to larger scales to assess whether the similarity between the distributions of ICL and mass holds at larger cluster radius. In this sense, The Beyond Ultra-deep Frontier Fields And Legacy Observations (BUFFALO, GO:15117, PI: Steinhardt), an extension of the HFF survey, will provide a wider view of these clusters allowing us to explore the ICL extending out to the edges of the massive HFF clusters. Also, current and future facilities like HSC, LSST, or *WFIRST* will provide wider field of views and statistics to study how the ICL traces the structures of groups and clusters in a wider range of total masses.

ACKNOWLEDGEMENTS

We thank the anonymous referee for their comments that helped to improve this manuscript. We would also like to thank STScI directors M. Mountain, K. Sembach, and J. Lotz, and all the HFF team for making these extraordinary data available. MM thanks Sarah Brough and Priya Natarajan for their support and helpful discussions. Support for this work was provided by NASA through grant *HST*-AR-14304 from the Space Telescope Science Institute, operated by AURA, Inc. under NASA contract NAS 5-26555 and by the Spanish Ministerio de Economía y Competitividad (MINECO; grant AYA2016-77237-C3-1-P). IT acknowledges financial support from the European Union's Horizon 2020 research and innovation programme under Marie Sklodowska-Curie grant agreement No 721463 to the SUNDIAL ITN network. This work utilizes gravitational lensing models produced by PIs BradaŽc, Natarajan & Kneib (CATS), Merten & Zitrin, Sharon, Williams, Keeton, Bernstein and Diego, and the GLAFIC group. This lens modelling was partially funded by the *HST* Frontier Fields programme conducted by STScI. STScI is operated by the Association of Universities for Research in Astronomy, Inc. under NASA contract NAS 5-26555. The lens models were obtained from the Mikulski Archive for Space Telescopes (MAST). This work makes extensive use of the following software: ASTROPY (Astropy Collaboration 2013; The Astropy Collaboration 2018), SExtractor (Bertin & Arnouts 1996), NUMPY (Jones et al. 2001; Oliphant 2007), SCIPY (Jones et al. 2001; Oliphant 2007), MATPLOTLIB (Hunter 2007).

REFERENCES

Annunziatella M. et al., 2017, ApJ, 851, 81
Astropy Collaboration, 2013, A&A, 558, A33
Balestra I. et al., 2016, ApJS, 224, 33
Bertin E., Arnouts S., 1996, A&AS, 117, 393
Borgani S., Guzzo L., 2001, Nature, 409, 39
Bradač M. et al., 2009, ApJ, 706, 1201
Burke C., Hilton M., Collins C., 2015, MNRAS, 449, 2353
Caminha G. B. et al., 2017, A&A, 600, A90
Clowe D., Gonzalez A., Markevitch M., 2004, ApJ, 604, 596
Cooper A. P., Gao L., Guo Q., Frenk C. S., Jenkins A., Springel V., White S. D. M., 2015, MNRAS, 451, 2703
Diego J. M., Broadhurst T., Molnar S. M., Lam D., Lim J., 2015a, MNRAS, 447, 3130
Diego J. M., Broadhurst T., Zitrin A., Lam D., Lim J., Ford H. C., Zheng W., 2015b, MNRAS, 451, 3920
Diego J. M. et al., 2016a, MNRAS, 456, 356
Diego J. M., Broadhurst T., Wong J., Silk J., Lim J., Zheng W., Lam D., Ford H., 2016b, MNRAS, 459, 3447
Diego J. M. et al., 2018, MNRAS, 473, 4279
Dubinski J., 1998, ApJ, 502, 141
Dubuisson M.-P., Jain A. K., 1994, A Modified Hausdorff Distance for Object Matching, Proc. 12th IAPR Int. Conf. Pattern Recognit., p. 566
Duc P.-A. et al., 2015, MNRAS, 446, 120
Ebeling H., Barrett E., Donovan D., Ma C.-J., Edge A. C., van Speybroeck L., 2007, ApJ, 661, L33
Edge A. C., Ebeling H., Bremer M., Röttgering H., van Haarlem M. P., Rengelink R., Courtney N. J. D., 2003, MNRAS, 339, 913
Ford H. C. et al., 1998, in Bely P. Y., Breckinridge J. B., eds, Proc. SPIE Conf. Ser. Vol. 3356, Space Telescopes and Instruments V. SPIE, Bellingham, p. 234
Gao L., White S. D. M., Jenkins A., Stoehr F., Springel V., 2004, MNRAS, 355, 819
Gómez P. L. et al., 2012, AJ, 144, 79
Goodwin S. P., Gribbin J., Hendry M. A., 1998, Observatory, 118, 201
Gregg M. D., West M. J., 1998, Nature, 396, 549
Grillo C. et al., 2015, ApJ, 800, 38
Hoag A. et al., 2016, ApJ, 831, 182
Hoekstra H., Bartelmann M., Dahle H., Israel H., Limousin M., Meneghetti M., 2013, Space Sci. Rev., 177, 75
Huang S., Leauthaud A., Greene J. E., Bundy K., Lin Y.-T., Tanaka M., Miyazaki S., Komiyama Y., 2018, MNRAS, 475, 3348
Hunter J. D., 2007, Comput. Sci. Eng., 9, 90
Huttenlocher D. P., Klanderman G. A., Rucklidge W. A., 1993, IEEE Trans. Pattern Anal. Mach. Intell., 15, 850
Iodice E. et al., 2017, ApJ, 851, 75
Ishigaki M., Kawamata R., Ouchi M., Oguri M., Shimasaku K., Ono Y., 2015, ApJ, 799, 12
Jauzac M. et al., 2014, MNRAS, 443, 1549
Jauzac M. et al., 2015a, MNRAS, 446, 4132
Jauzac M. et al., 2015b, MNRAS, 452, 1437
Jauzac M. et al., 2016a, MNRAS, 457, 2029
Jauzac M. et al., 2016b, MNRAS, 463, 3876
Jiménez-Teja Y. et al., 2018, ApJ, 857, 79
Johnson T. L., Sharon K., Bayliss M. B., Gladders M. D., Coe D., Ebeling H., 2014, ApJ, 797, 48
Jones E. et al., 2001, SciPy: Open source scientific tools for Python, Available at: http://www.scipy.org/
Jullo E., Kneib J.-P., 2009, MNRAS, 395, 1319
Kartaltepe J. S., Ebeling H., Ma C. J., Donovan D., 2008, MNRAS, 389, 1240
Kawamata R., Oguri M., Ishigaki M., Shimasaku K., Ouchi M., 2016, ApJ, 819, 114
Kawamata R., Ishigaki M., Shimasaku K., Oguri M., Ouchi M., Tanigawa S., 2018, ApJ, 855, 4
Keeton C. R., 2010, Gen. Relativ. Gravit., 42, 2151
Kneib J.-P., Natarajan P., 2011, A&AR, 19, 47
Krick J. E., Bernstein R. A., 2007, AJ, 134, 466
Lagattuta D. J. et al., 2017, MNRAS, 469, 3946
Lam D., Broadhurst T., Diego J. M., Lim J., Coe D., Ford H. C., Zheng W., 2014, ApJ, 797, 98
Liesenborgs J., De Rijcke S., Dejonghe H., 2006, MNRAS, 367, 1209

Limousin M. et al., 2016, A&A, 588, A99
Lotz J. M. et al., 2017, ApJ, 837, 97
McGaugh S. S., 2015, Can. J. Phys., 93, 250
MacKenty J. W., Kimble R. A., O'Connell R. W., Townsend J. A., 2008, Proc. SPIE, Vol. 7010, Space Telescopes and Instrumentation 2008: Optical, Infrared, and Millimeter, p. 70101F
Mahler G. et al., 2018, MNRAS, 473, 663
Ma C.-J., Ebeling H., Barrett E., 2009, ApJ, 693, L56
Mann A. W., Ebeling H., 2012, MNRAS, 420, 2120
Markevitch M., Gonzalez A. H., Clowe D., Vikhlinin A., Forman W., Jones C., Murray S., Tucker W., 2004, ApJ, 606, 819
Meneghetti M. et al., 2017, MNRAS, 472, 3177
Merten J., Cacciato M., Meneghetti M., Mignone C., Bartelmann M., 2009, A&A, 500, 681
Merten J. et al., 2011, MNRAS, 417, 333
Mihos J. C., 2016, in Bragaglia A., Arnaboldi M., Rejkuba M., Romano D., eds, Proc. IAU Symp. 317, The General Assembly of Galaxy Halos: Structure, Origin and Evolution. p. 27
Mihos J. C., Harding P., Feldmeier J., Morrison H., 2005, ApJ, 631, L41
Milgrom M., 2002, New Astron. Rev., 46, 741
Montes M., Trujillo I., 2014, ApJ, 794, 137
Montes M., Trujillo I., 2018, MNRAS, 474, 917 (MT18)
Natarajan P. et al., 2017, MNRAS, 468, 1962
Navarro J. F., Frenk C. S., White S. D. M., 1996, ApJ, 462, 563
Navarro J. F., Frenk C. S., White S. D. M., 1997, ApJ, 490, 493
Oguri M., 2010, PASJ, 62, 1017
Oliphant T. E., 2007, Comput. Sci. Eng., 9, 10
Owers M. S., Randall S. W., Nulsen P. E. J., Couch W. J., David L. P., Kempner J. C., 2011, ApJ, 728, 27
Paczynski B., 1987, Nature, 325, 572
Pillepich A. et al., 2014, MNRAS, 444, 237
Pillepich A. et al., 2018, MNRAS, 475, 648
Planck Collaboration XIII, 2016, A&A, 594, A13
Priewe J., Williams L. L. R., Liesenborgs J., Coe D., Rodney S. A., 2017, MNRAS, 465, 1030
Primack J. R., Blumenthal G. R., 1984, in Audouze J., Tran Thanh Van J., eds, NATO Advanced Science Institutes (ASI) Series C Vol. 117, NATO Advanced Science Institutes (ASI) Series C. p. 163
Remolina González J. D., Sharon K., Mahler G., 2018, ApJ, 863, 60
Richard J., Kneib J.-P., Limousin M., Edge A., Jullo E., 2010, MNRAS, 402, L44
Richard J. et al., 2014, MNRAS, 444, 268
Sebesta K., Williams L. L. R., Mohammed I., Saha P., Liesenborgs J., 2016, MNRAS, 461, 2126
Soucail G., Fort B., Mellier Y., Picat J. P., 1987, A&A, 172, L14
The Astropy Collaboration, 2018, ApJ, 156, 123
Trujillo I., Fliri J., 2016, ApJ, 823, 123
van Weeren R. J. et al., 2017, ApJ, 835, 197
Williams L. L. R., Sebesta K., Liesenborgs J., 2018, MNRAS, 480, 3140
Zitrin A., Broadhurst T., 2009, ApJ, 703, L132
Zitrin A., Broadhurst T., Bartelmann M., Rephaeli Y., Oguri M., Benítez N., Hao J., Umetsu K., 2012, MNRAS, 423, 2308
Zitrin A. et al., 2013, ApJ, 762, L30
Zitrin A. et al., 2015, ApJ, 801, 44
Zwicky F., 1933, Helv. Phys. Acta, 6, 110
Zwicky F., 1937, ApJ, 86, 217

APPENDIX A: MHD VALUES

We provide the median MHD values in kpc for the five different radial distances from the centres of the mass/light distributions: 50, 75, 100, 125, and 140 kpc (see Section 3 for more details in the choice of the centre and derivation of the isocontours). Table A1 has the MHD values for the comparison among the ICL and the different mass models, Table A2 for the comparison among the different mass models and Table A3 for the comparison among the X-rays emission and the mass models.

Table A1. Median MHD values and standard deviations of the comparison of the ICL with the different mass models. MHD is given in kpc.

R (kpc)	A2744	M0416	M0717	M1149	AS1063	A370
50	8.1 ± 12.3	11.0 ± 6.5	35.3 ± 19.4	14.3 ± 32.5	4.6 ± 21.2	21.7 ± 7.0
75	20.8 ± 4.9	11.4 ± 6.0	41.5 ± 16.8	33.1 ± 17.6	9.5 ± 14.2	20.0 ± 4.7
100	25.0 ± 5.0	16.5 ± 10.1	35.8 ± 6.2	32.8 ± 14.6	15.5 ± 9.3	24.1 ± 4.0
125	31.0 ± 4.8	20.8 ± 9.0	41.2 ± 10.8	27.4 ± 11.7	20.8 ± 6.0	36.0 ± 8.9
140	32.9 ± 5.6	34.9 ± 7.3	41.0 ± 14.3	36.9 ± 9.3	23.8 ± 6.3	35.6 ± 10.9

Table A2. Median MHD values and standard deviations of the comparison among the different mass models. MHD is given in kpc.

R (kpc)	A2744	M0416	M0717	M1149	AS1063	A370
50	9.8 ± 13.3	10.3 ± 2.9	62.1 ± 32.2	58.4 ± 30.8	7.9 ± 2.4	18.7 ± 10.5
75	21.3 ± 10.1	12.2 ± 4.0	45.7 ± 20.7	54.5 ± 24.6	18.6 ± 18.7	18.6 ± 10.6
100	29.5 ± 10.2	17.5 ± 6.1	39.9 ± 12.3	48.5 ± 17.7	31.7 ± 15.8	31.6 ± 10.9
125	29.1 ± 11.1	22.0 ± 15.3	41.5 ± 19.9	43.5 ± 16.0	32.0 ± 13.0	32.6 ± 12.3
175	32.1 ± 10.8	33.8 ± 12.9	52.2 ± 23.7	40.7 ± 15.8	26.3 ± 9.7	34.8 ± 9.3

Table A3. Median MHD values and standard deviations of the comparison of the X-rays and the mass model distributions. MHD is given in kpc.

R (kpc)	A2744	M0416	M0717	M1149	AS1063	A370
50	134.9 ± 16.5	27.3 ± 9.0	231.3 ± 28.3	63.5 ± 12.3	23.5 ± 12.0	31.3 ± 5.6
75	93.2 ± 12.6	25.5 ± 2.5	187.5 ± 31.9	55.2 ± 18.3	28.3 ± 6.5	25.3 ± 5.0
100	121.9 ± 19.5	32.8 ± 7.8	56.0 ± 8.1	48.7 ± 21.1	32.8 ± 11.4	25.2 ± 4.7
125	116.9 ± 18.5	33.6 ± 7.4	52.0 ± 12.9	48.4 ± 17.2	41.3 ± 7.7	28.0 ± 6.9
140	109.5 ± 22.7	40.7 ± 5.0	43.1 ± 19.3	58.0 ± 10.7	42.1 ± 7.3	36.4 ± 4.7

This paper has been typeset from a TEX/LATEX file prepared by the author.